Chemical Science

ROYAL SOCIETY OF CHEMISTRY

EDGE ARTICLE

View Article Online
View Journal | View Issue

Cite this: *Chem. Sci.*, 2025, **16**, 11970

All publication charges for this article have been paid for by the Royal Society of Chemistry

Received 10th April 2025
Accepted 24th May 2025

DOI: 10.1039/d5sc02658j

rsc.li/chemical-science

Industrial electrooxidation of glutaraldehyde waste to glutaric acid *via* tailoring OH* coverage†

Jiani Han,[ab] Yaodong Yu,[a] Yingying Wei,[ac] G. A. Bagliuk,[d] Jingqi Chi,[a] Jianping Lai *[a] and Lei Wang *[a]

Glutaric acid (GA) is an important organic chemical raw material, but current industrialized production routes suffer from process complexity, low yield, and the use of high-polluting oxidants. Electrocatalytic synthesis of GA from glutaraldehyde waste provides a sustainable alternative to highly polluting conventional production methods. However, industrial production still faces challenges such as low energy efficiency (EE) and selectivity. Here, we present a commercially feasible GA electrosynthesis strategy with an EE of 55.4%, which significantly exceeds the 34.8% EE deemed economically viable based on a technical–economic analysis. We demonstrate that the high selectivity of glutaric acid (97%) is achieved through hydroxyl spillover from the introduction of Fe, which reduces the OH* coverage on the NiOOH site to inhibit the over-oxidation of glutaraldehyde. The bifunctional electrocatalyst-catalyzed HER–GOR system exhibits high Faraday efficiencies at both electrodes (99.8% for the HER and 92.7% for the GOR) and excellent stability after 24 hours of continuous operation at 500 mA cm^{-2}, achieving an EE of 55.4%.

Introduction

In recent years, the development of green processes for the production of glutaric acid (GA) has garnered significant attention due to its importance as a high-value organic chemical with a wide range of applications in medical, construction, pharmaceutical, agricultural, and biological fields.[1–4] The global market for GA is projected to reach $1982 million by 2029, driven by the growing demand in the pharmaceutical industry. However, traditional methods for GA production, which involve the conversion of cyclopentanol, cyclopentanone, and 1,4-butyrolactone, are plagued by the use of harsh conditions, high-polluting oxidants, and costly catalysts.[5] These conventional approaches are not only environmentally detrimental but also economically unsustainable. Electrochemical methods, in contrast, offer a sustainable alternative for GA synthesis by leveraging renewable electricity to drive the oxidation of glutaraldehyde waste, thereby eliminating the need for hazardous chemical reagents.[6–11] The industrial feasibility of this electrosynthesis route hinges on optimizing key performance metrics, with energy efficiency (EE) being a critical factor.[12–14] The techno-economic analysis indicates that achieving an EE of over 34.8% is essential for commercial viability at industrial current densities (Fig. 1a and b).

To enhance EE, it is crucial to improve the selectivity of GA production.[12] Alkaline electrolytes, which promote the generation of active oxygen species, are often used in electrocatalytic anodic organic oxidation reactions.[15–17] Conventional electrocatalytic oxidation of aldehydes is facilitated by increasing OH* species, thereby achieving enhanced faradaic efficiency (FE) and reduced energy barriers.[16,18] However, the available electrooxidation pathways for open-chain aldehydes typically result in reactant degradation, as excess OH* leads to excessive oxidation of the aldehyde and C–C bond cleavage, generating low-value CO_2.[19–22] The adsorption energy of reaction intermediates is also influenced by the applied potential, which in turn affects the reaction pathway and selectivity.[23] According to Sabatier's principle, the interaction between the catalyst and the reaction intermediates should be moderate to achieve efficient catalysis.[24] Thus, strategies to inhibit over-oxidation and C–C bond cleavage, while optimizing adsorption–desorption, are necessary to achieve high GA selectivity and commercialize electrocatalytic GA production.[25]

In this study, we present an efficient GA electrosynthesis strategy that achieves high selectivity (97%) and commercial

[a]*State Key Laboratory Base of Eco-Chemical Engineering, Ministry of Education, International Science and Technology Cooperation Base of Eco-chemical Engineering and Green Manufacturing, College of Chemistry and Molecular Engineering, Qingdao University of Science and Technology, Qingdao 266042, P. R. China. E-mail: jplai@qust.edu.cn; inorchemwl@126.com*

[b]*Shandong Engineering Research Center for Marine Environment Corrosion and Safety Protection, College of Environment and Safety Engineering, Qingdao University of Science and Technology, Qingdao 266042, P. R. China*

[c]*College of Chemical Engineering, Qingdao University of Science and Technology, Qingdao 266042, P. R. China*

[d]*Frantsevich Institute for Problems of Materials Science National Academy of Sciences of Ukraine, Kyiv 02000, Ukraine*

† Electronic supplementary information (ESI) available. See DOI: https://doi.org/10.1039/d5sc02658j

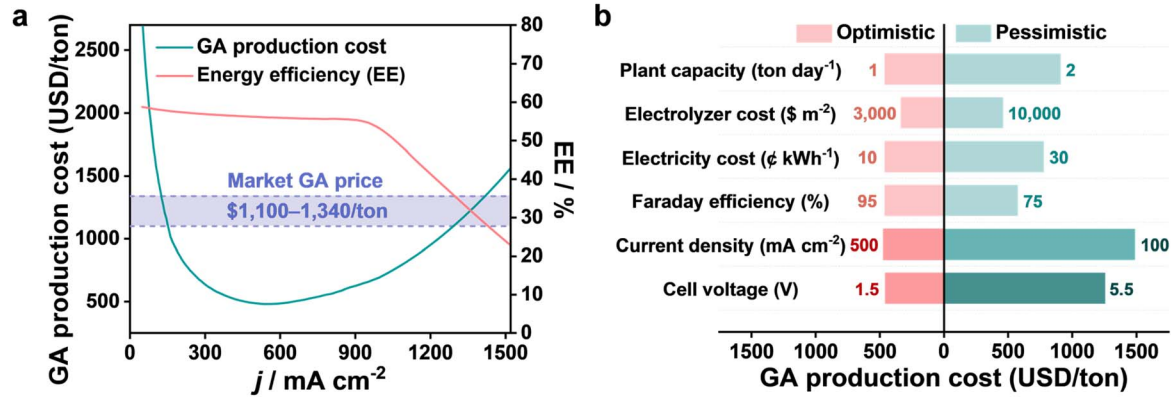

Fig. 1 Techno-economic analysis of GA electrosynthesis. (a) The relationship between electrochemical GA production cost and current density; and the corresponding EE at various current densities. (b) Univariate sensitivity analysis of GA production costs. The optimistic and pessimistic parameters shown in the figure were chosen based on the calculations in this work.

viability with an EE of 55.4%. Computational and *in situ* spectroscopic investigations reveal that the introduction of Fe into the NiOOH site enhances the adsorption and conversion of glutaraldehyde. Specifically, hydroxyl spillover from Fe effectively reduces the OH* coverage on NiOOH, inhibiting the over-oxidation of glutaraldehyde and suppressing C–C bond cleavage. Additionally, Fe regulates the electronic structure of the catalyst, modulating the adsorption of intermediates and lowering the energy barrier of the rate-determining step. The glutaraldehyde-assisted water electrolyzer demonstrates significant long-term stability, achieving high FEs for GA (92.7%) and H_2 (99.8%) over 24 hours of continuous operation at an industrial current density of 500 mA cm^{-2}. Based on techno-economic analysis, the cost of industrial GA electrosynthesis is estimated to be US$472 per ton, which is only about 0.43 of the lowest market price (US$1100 per ton). Our work provides a promising strategy for the industrialization and economic viability of glutaraldehyde waste electrocatalytic oxidation into high-value-added GA.

Results and discussion

Synthesis and characterization of catalysts

Electrocatalysts were synthesized on copper foam (CF) substrates through an electrodeposition method using cost-effective iron and nickel nitrate salts, with the fabrication process detailed in Fig. S1.† The morphological features of the deposits were characterized by scanning electron microscopy (SEM) and transmission electron microscopy (TEM). SEM imaging revealed a smooth, flat surface on pristine Cu foam (Fig. S2†), while after electrodeposition, the 3D CF skeleton became uniformly coated with Fe, Ni, and FeNi deposits (designated as Fe/CF, Ni/CF, and $Fe_{0.5}Ni$/CF), forming a rough surface morphology distinct from bare CF (Fig. 2a, b and S3†). To eliminate interference from the Cu foam substrate during characterization, electrodeposited materials were detached *via* ultrasonication. TEM analysis of $Fe_{0.5}Ni$/CF (Fig. 2c) provided microstructural insights, while inductively coupled plasma-atomic emission spectroscopy (ICP-AES) confirmed an Fe/Ni atomic ratio of 1 : 2 (Table S1†). X-ray diffraction (XRD) patterns of ultrasonically removed Fe, Ni (Fig. S4†), and $Fe_{0.5}Ni$ (Fig. 2d) powders matched standard peaks for metallic Ni (PDF#70-1849) and Fe (PDF#85-1410). The $Fe_{0.5}Ni$ pattern exhibited negatively shifted Ni diffraction peaks corresponding to (111), (200), and (220) planes, indicating lattice expansion due to Fe incorporation.[26] The prominent peaks near 44° were attributed to Ni (111) and Fe (110) facets, consistent with HRTEM observations showing lattice spacings of 0.204 nm (Ni (111)) and 0.203 nm (Fe (110)) (Fig. 2e). X-ray photoelectron spectroscopy (XPS) analysis of $Fe_{0.5}Ni$ powder revealed mixed oxidation states: Ni spectra showed peaks for Ni^0 (852.9 eV, 870.7 eV), Ni^{2+} (856.0 eV, 874.3 eV), and Ni^{3+} (859.1 eV, 877.4 eV), while Fe spectra contained Fe^0 (705.9 eV, 721.5 eV), Fe^{2+} (710.1 eV, 723.8 eV), and Fe^{3+} (714.2 eV, 726.0 eV) species (Fig. 2f and S5†).[27,28] HAADF-STEM and EDS mapping confirmed the homogeneous distribution of Fe and Ni throughout the catalyst (Fig. 2g).

Electrocatalytic performance and product analysis

The oxygen evolution reaction (OER) is the primary competing process during glutaraldehyde electrochemical oxidation. To assess the glutaraldehyde oxidation reaction (GOR) and OER activities of $Fe_{0.5}Ni$/CF, linear sweep voltammetry (LSV) was performed in a three-electrode system using 1.0 M KOH with and without 0.01 M glutaraldehyde (Fig. 3a). The selected glutaraldehyde concentration (0.01 M) reflects environmental concerns, as residual glutaraldehyde from wastewater discharges may harm marine organisms.[29] LSV results revealed an OER onset potential of 1.51 V *vs.* RHE for $Fe_{0.5}Ni$/CF. Upon adding glutaraldehyde, the onset potential shifted negatively by 210 mV to 1.30 V *vs.* RHE, demonstrating preferential catalytic conversion of glutaraldehyde over water oxidation due to thermodynamic favorability. Polarization curves of $Fe_{0.5}Ni$/CF, Ni/CF, Fe/CF, and CF in 1.0 M KOH + 0.01 M glutaraldehyde (Fig. 3b) showed $Fe_{0.5}Ni$/CF achieving the lowest onset potential (1.29 V *vs.* RHE) compared to Ni/CF (1.35 V) and Fe/CF (1.40 V). At 100 mA cm^{-2}, $Fe_{0.5}Ni$/CF required only 1.44 V, outperforming

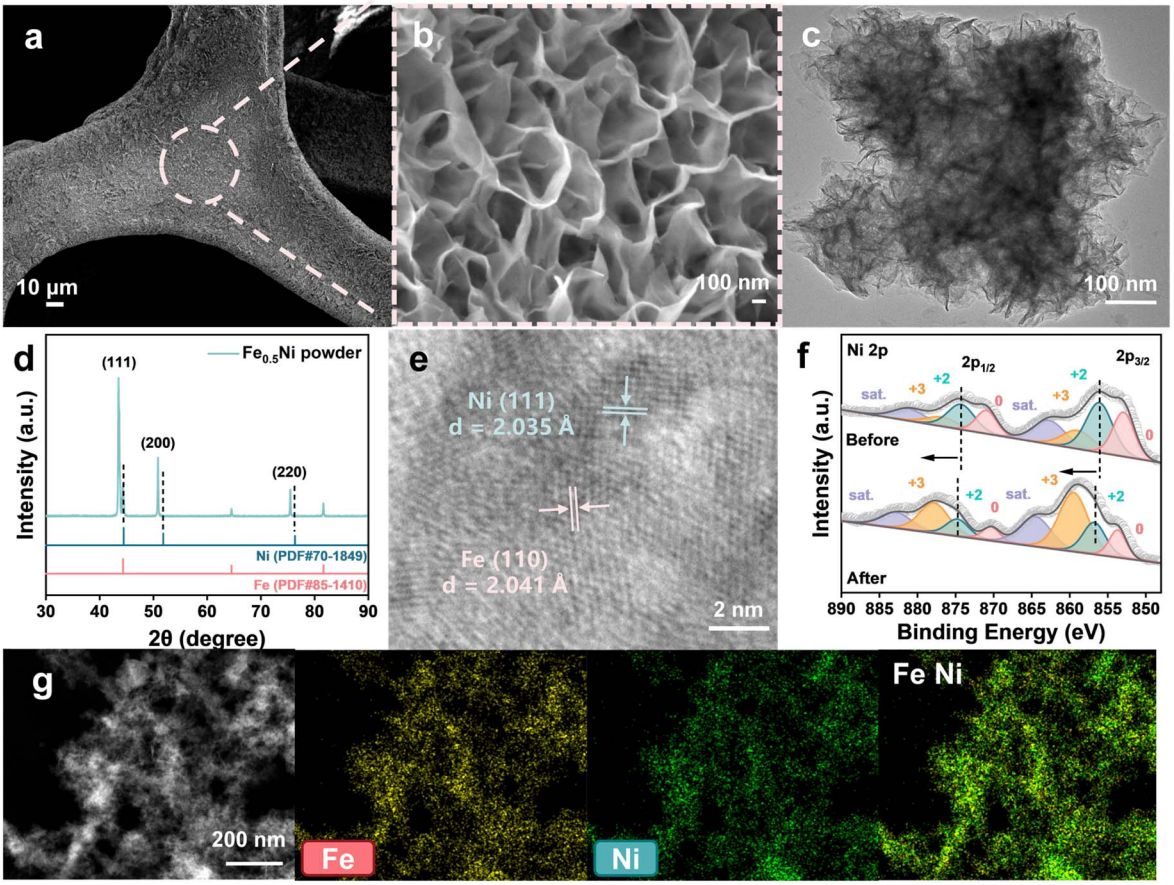

Fig. 2 Morphology characterization. (a) and (b) SEM images of as-deposited $Fe_{0.5}Ni$/CF catalyst. (c) TEM image of $Fe_{0.5}Ni$. (d) XPS spectra of Ni 2p for $Fe_{0.5}Ni$ prior to and post electrolysis at 1.38 V *vs.* RHE. (e) HRTEM image of $Fe_{0.5}Ni$. (f) XRD pattern of $Fe_{0.5}Ni$ powder. (g) HAADF-STEM image and corresponding elemental mappings of Fe and Ni for $Fe_{0.5}Ni$.

Ni/CF (1.49 V) and Fe/CF (1.54 V). Electrochemical active surface area (ECSA) analysis *via* double-layer capacitance (C_{dl}) measurements (Fig. S6a–c†) indicated that $Fe_{0.5}Ni$/CF exhibited the highest C_{dl} (4.25 mF cm^{-2}) and ECSA (106.25 cm^2), surpassing Ni/CF (2.06 mF cm^{-2}, 71.25 cm^2) and Fe/CF (2.85 mF cm^{-2}, 51.50 cm^2), suggesting greater exposure of active sites (Fig. S6d and e†). Specific activity (ECSA-normalized current density) is applied to investigate the intrinsic activity of the catalyst.[30,31] Fig. S7a† suggests that the activity of $Fe_{0.5}Ni$/CF is higher than that of the other samples. The large increase in the specific activity of $Fe_{0.5}Ni$/CF reveals that the performance improvement results from both the increase in ECSA and the enhancement of intrinsic activity. Moreover, the overpotentials of specific activity normalized by ECSA for $Fe_{0.5}Ni$/CF are much lower than those for Ni/CF and Fe/CF (Fig. S7b†). Electrochemical impedance spectroscopy (EIS) further confirmed $Fe_{0.5}Ni$/CF's superior charge-transfer efficiency (Fig. S8†), aligning with LSV trends. Notably, $Fe_{0.5}Ni$/CF demonstrated optimal performance for both glutaric acid production at the anode and hydrogen evolution at the cathode, maintaining the hierarchy: $Fe_{0.5}Ni$/CF > Ni/CF > Fe/CF > CF (Fig. 3c). This confirms $Fe_{0.5}Ni$/CF's dual functionality in GOR and HER applications.

While achieving high catalytic activity is essential, stability remains a critical parameter for practical implementation. Stability tests on $Fe_{0.5}Ni$/CF in 1.0 M KOH + 0.01 M glutaraldehyde at 1.38 V *vs.* RHE demonstrated consistent current profiles over five consecutive electrolysis cycles (Fig. S9a†), with glutaraldehyde (GA) yield and FE retaining 93.7% and 92.9%, respectively, confirming robust stability for the GOR (Fig. S9b†). Polarization curves of $Fe_{0.5}Ni$/CF remained nearly unchanged after 10 000 CV cycles (Fig. S10a and b†), while chronoamperometric testing in 1.0 M KOH over 120 h revealed stable current density at 100 mA cm^{-2}, indicating no significant performance degradation (Fig. S10c†). Post-stability analysis showed only minor decreases in C_{dl} and ECSA (Fig. S11†), and XRD patterns retained their original features (Fig. S12†), further validating structural integrity. XPS analysis post-stability testing revealed a positive shift in Ni 2p peaks toward higher oxidation states (Fig. 2f), reflecting electron loss from Ni and an increased Ni^{3+} : Ni^{2+} ratio, consistent with oxidative reconstruction during the GOR. SEM imaging confirmed preserved morphology after stability testing (Fig. S13†). These results collectively highlight $Fe_{0.5}Ni$/CF's exceptional stability as a critical electrocatalyst attribute.

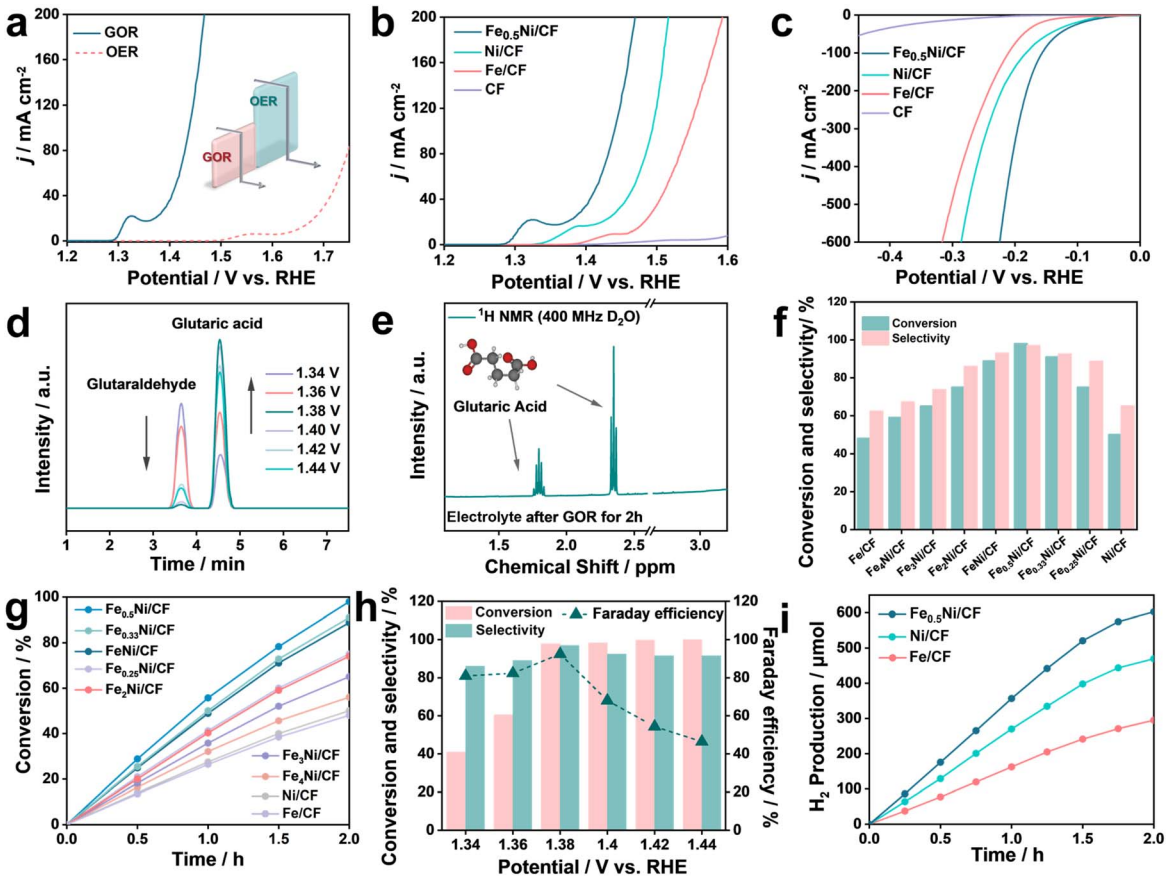

Fig. 3 Electrocatalytic performance and product analysis. (a) Linear sweep voltammetry curves of $Fe_{0.5}Ni/CF$ at the anode in 1.0 M KOH electrolyte with and without 0.01 M glutaraldehyde. (b) LSV curves of $Fe_{0.5}Ni/CF$, Fe/CF, Ni/CF, and CF in 1.0 M KOH + 0.01 M glutaraldehyde electrolyte. (c) Comparison of the LSV of four catalysts at the cathode in 1 M KOH solution. (d) HPLC chromatograms acquired at various electrolysis potentials. (e) ^1H NMR spectra of the anodic product obtained through the upgraded electrooxidation of glutaraldehyde by chronoamperometry (*I*–*t*) at 1.38 V *vs.* RHE for 2 hours. (f) The comparison of glutaraldehyde conversion and selectivity of varied electrodes at 1.38 V *vs.* RHE. (g) Glutaraldehyde conversion with time for different electrodes. (h) The conversion, selectivity, and FE of glutaraldehyde under changed applied potentials on the $Fe_{0.5}Ni/CF$ catalyst. (i) Comparison of H_2 amounts measured experimentally over time with different electrodes.

Organic products in the anode chamber's liquid phase were identified and quantified *via* high-performance liquid chromatography (HPLC) and ^1H nuclear magnetic resonance (NMR). HPLC analysis quantified glutaric acid production across different electrolysis potentials (Fig. 3d), supported by a calibration curve (Fig. S14†). ^1H NMR results using DMSO as an internal standard aligned with HPLC data, showing characteristic glutaric acid peaks at 1.79 and 2.33 ppm (Fig. 3e), with a corresponding calibration curve (Fig. S15†). The conversion, selectivity, and yield of GA depended on the Fe/Ni ratio in the electrodes (Fig. 3f and S16a†). Fig. S16b† shows that after 2 h of electrolysis, the FEs of GA decrease with the increase of the Fe : Ni ratio. Similarly, the GA FEs are decreased by increasing the Ni content, yet the main by-products' (CO_2 and HCOOH) FEs are increased. The experimental results suggest that an Fe : Ni ratio of 0.5 : 1 provides the best catalytic performance for the GOR. Notably, after 2 h of electrocatalysis, the difference between Ni/CF and Fe/CF was slight, so the electrocatalytic duration was prolonged to explore the roles of Fe and Ni (Fig. S17a and b†). The gradual increase in CO_2 FEs on Ni/CF is due to the lack of the OH* spillover effect from Fe sites and excess OH*, leading to over-oxidation. On Fe/CF, the significant increase in CO_2 FEs was attributed to the higher OH* coverage on Fe sites, thus demonstrating that Fe fails to act as an active site for the GOR.[32] Systematic poisoning experiments were further performed to investigate the effect of the Ni and Fe sites in $Fe_{0.5}Ni/CF$ for the GOR (Fig. S17c†). Thiocyanate ion (SCN^-) and oxalate ($C_2O_4^-$) were utilized to selectively block Ni and Fe sites, respectively.[33,34] The FE_{GA} decrease of the blocked Ni site sample is minor compared to the blocked Fe site sample, suggesting that the Ni site is the active site. Furthermore, the GOR catalytic performance of other noble/non-precious metal catalysts was investigated. It is found that $Fe_{0.5}Ni/CF$ significantly inhibits the side reactions through the bimetallic synergistic effect and realizes the efficient glutaraldehyde electrooxidation (Fig. S18†). At 1.38 V *vs.* RHE, $Fe_{0.5}Ni/CF$ achieved optimal glutaraldehyde conversion (Fig. 3g), outperforming other electrodes. GA metrics (FE, conversion, selectivity, yield) were potential-dependent (1.34–1.44 V *vs.* RHE; Fig. 3h and S19†), with $Fe_{0.5}Ni/CF$ delivering peak FE (94.3%), selectivity (97.0%), and

yield (95.0%) at 1.38 V. Minor by-products (formic acid, CO_2) were detected. FE variation with KOH concentration is shown in Fig. S20.† Within a range of KOH concentrations, due to the OH* spillover effect of Fe, which can effectively adsorb excess OH* at the Ni site, high glutaraldehyde oxidation efficiencies are maintained. With the reduction of KOH concentration (0.5 M and 0 M), OH* species were consequently reduced, hindering the glutaraldehyde oxidation due to insufficient nucleophilic attack of oxidized species OH*, thus decreasing the FEs of GA. $Fe_{0.5}Ni/CF$ also exhibited superior H_2 production (Fig. 3i), validated by gas chromatography (GC; Fig. S21†), with experimental H_2 yields matching theoretical calculations. Comparative analysis (Table S2†) highlights $Fe_{0.5}Ni/CF$'s superior performance in anodic aldehyde upgrading relative to prior reports.

Industrial-scale GA electrosynthesis

To evaluate catalyst performance under realistic conditions, a two-compartment electrochemical cell separated by an anion-exchange membrane (AEM) was employed, with $Fe_{0.5}Ni/CF$ serving as both anode and cathode (Fig. 4a). This paired electrolysis system integrates glutaraldehyde oxidation (GOR) to glutaric acid (GA) at the anode (1.0 M KOH + 0.01 M glutaraldehyde) with hydrogen evolution (HER) at the cathode (1.0 M KOH), enhancing energy efficiency while generating valuable products. Linear sweep voltammetry (LSV) revealed superior performance for the HER–GOR system compared to HER–OER, with a pronounced current increase (Fig. S22†). Gas chromatography (GC) confirmed negligible oxygen production below 2.08 V, indicating GOR dominance over the OER at moderate voltages (Fig. S23†). Faradaic efficiencies (FEs) for GA and H_2

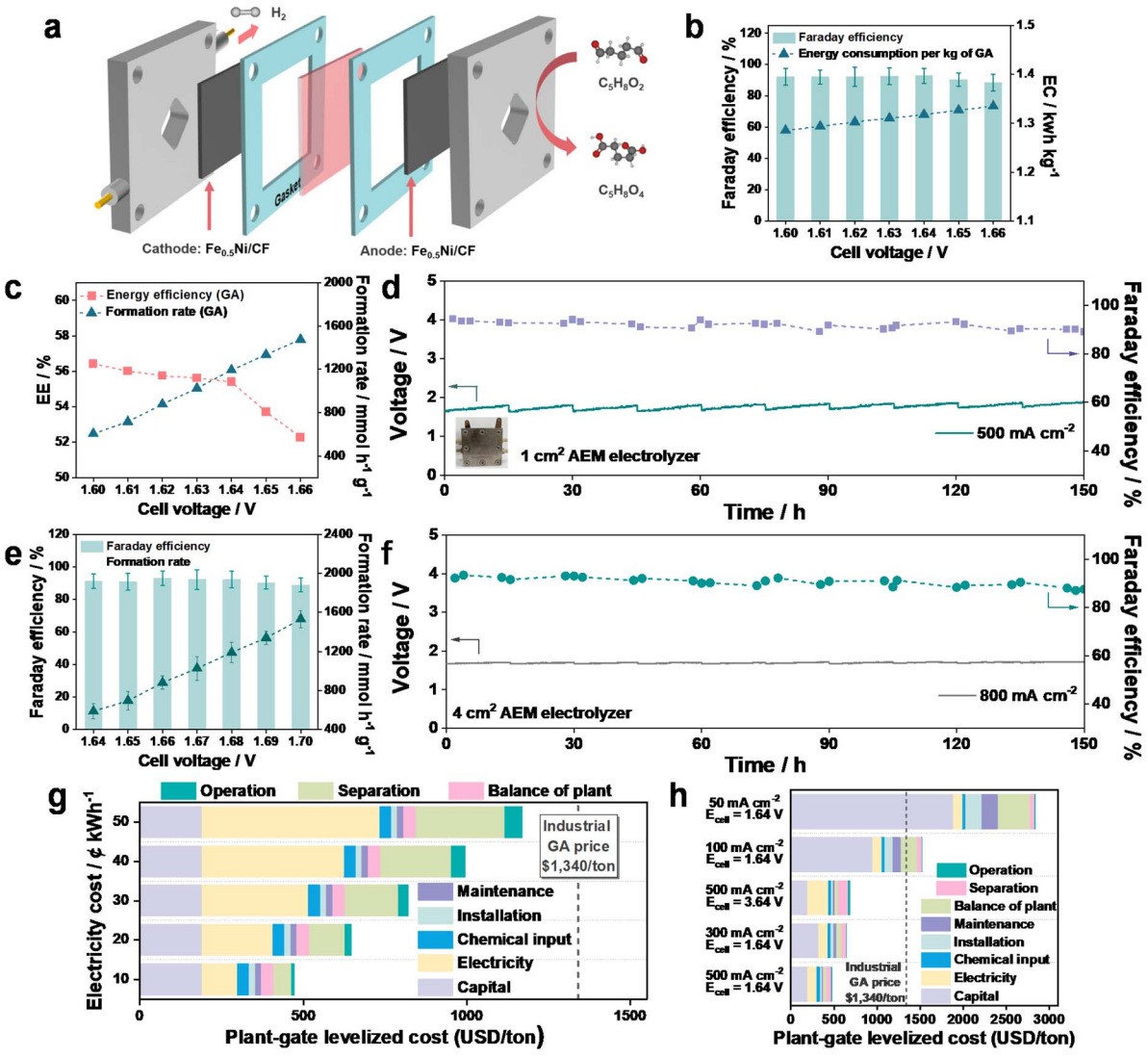

Fig. 4 AEM electrolyzer performance. (a) Architecture of the AEM electrolyzer. (b) FE and EC of GA at different cell voltages. (c) EE and formation rate of GA at various applied cell voltages. (d) A long-term chronopotentiometry curve under 500 mA cm^{-2} output for 24 h: cell voltage and FE_{GA} as a function of time. The inset is a digital photograph of the AEM electrolyzer. (e) GA FEs and formation rates at various applied cell voltages. (f) Stability test in a 4 cm^2 AEM electrolyzer at a current density of 800 mA cm^{-2}. Techno-economic analysis of GA electrosynthesis by the GOR (g) with different electricity costs and (h) under various conditions. The comparison parameters in (h) are based on the analysis in Fig. S26.†

remained high across varying cell voltages (Fig. 4b, S24a), though energy consumption (EC) for both products increased with voltage. Energy efficiency (EE) inversely correlated with voltage, while formation rates rose proportionally (Fig. 4c). Long-term stability testing at 500 mA cm^{-2} over 150 h demonstrated consistent performance, with GA FE stable at ~92% (Fig. 4d). The HER–GOR system reduced H_2 energy consumption to 43.54 kW h kg^{-1}, outperforming conventional HER–OER (48.34 kW h kg^{-1}), while maintaining H_2 FE near 99.8% (Fig. S24b†). GA production required only 1.32 kW h kg^{-1} with 92.7% FE. To evaluate the scalability of glutaraldehyde–GA electrocatalysis, the active area of the catalyst was expanded to 4 cm^2, achieving >90% FE over a wide range of voltages and 150 hours of stable operation at an industrial current density of 800 mA cm^{-2} (Fig. 4e and f). The system maintains >50% EE with low energy consumption, and a techno-economic analysis confirms its commercial viability, with production costs well below industrial GA market prices (Fig. S25†). Techno-economic analysis highlighted the feasibility of GA production using $Fe_{0.5}$Ni/CF, with plant-gate costs significantly below market prices (Fig. 4g, h, S26, Table S3†). Utilizing waste glutaraldehyde from disinfectant residues minimizes feedstock costs and environmental impact, enhancing both economic and ecological benefits. This approach not only addresses industrial demands but also mitigates environmental challenges associated with glutaraldehyde pollution. Life cycle assessment (LCA) principles were employed in this study to evaluate the environmental impacts of glutaraldehyde electrooxidation and electrodes (Fig. S27 and Table S4†).[35] The present electrocatalytic process can be improved using the options proposed in Table S5† to address possible environmental hazards to improve competitiveness.

Mechanism investigations

In situ Raman spectroscopy and density functional theory (DFT) calculations were employed to elucidate the atomic-level mechanisms of glutaraldehyde electro-oxidation. *In situ* Raman spectra collected in 1.0 M KOH + 0.01 M glutaraldehyde at 1.34–1.44 V *vs.* RHE reveal dual peaks at 477 cm^{-1} (Ni–O bending) and 558 cm^{-1} (Ni–O stretching), characteristic of NiOOH species (Fig. 5a and b).[36,37] Electrochemical reconstruction of $Fe_{0.5}$Ni/CF and Ni/CF electrodes formed $Fe_{0.5}$NiOOH and NiOOH, respectively, enhancing catalytic activity. Notably, the intensity of the two peaks for Ni/CF is rapidly enhanced with increasing applied potential compared to $Fe_{0.5}$Ni/CF. The apparent Raman signal at 746 cm^{-1} (attributed to Fe–OH species) exhibits a similar potential-dependent trend for the $Fe_{0.5}$Ni/CF (Fig. 5a).[38] These phenomena are attributed to that OH* is mainly adsorbed on Ni sites in Ni/CF catalysts, whereas the introduction of Fe into $Fe_{0.5}$Ni/CF facilitates the spillover of excess OH* to the Fe site, thus decreasing the OH* coverage on Ni sites and inhibiting the over-oxidation of reactants. As shown in Fig. 5c, the intensity of the Fe–OH peaks for Fe/CF catalysts enhances rapidly with increasing potential, indicating that OH* is more readily adsorbed on the Fe site.[39] Furthermore, the adsorption energy of OH* at the Fe site is much stronger than at the Ni site and is thermodynamically more stable (Fig. 5d). Strong adsorption results in the Fe site being occupied by OH*,

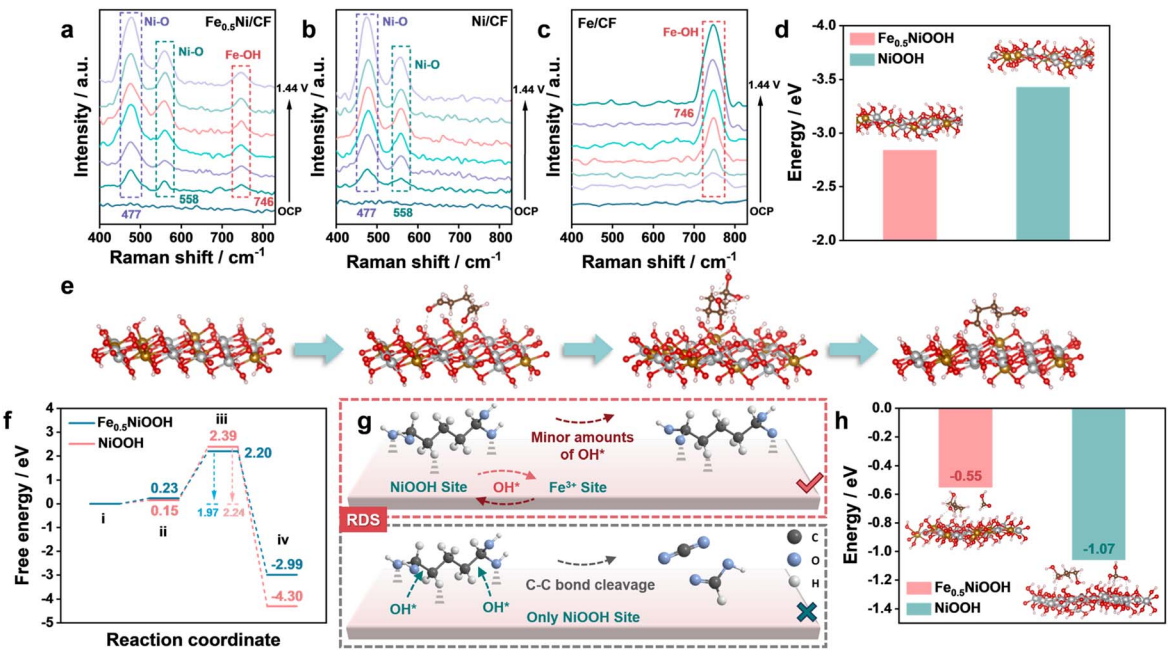

Fig. 5 Mechanistic studies. *In situ* Raman spectra of (a) $Fe_{0.5}$Ni/CF, (b) Ni/CF, and (c) Fe/CF recorded at different potentials during the GOR. (d) Free energy diagrams for OH* adsorption. (e) Optimized structures of adsorption configurations of reaction intermediates involved in the oxidation pathway of glutaraldehyde on $Fe_{0.5}$NiOOH sites. Color code: silver, Ni; gold, Fe; red, O; white, H; brown, C. (f) Free energy diagrams calculated for the oxidation of glutaraldehyde to glutaric acid on $Fe_{0.5}$NiOOH and NiOOH. (g) Proposed mechanism for the hydroxyl spillover strategy. (h) Dissociation energies of the C–C bond for RDS on $Fe_{0.5}$NiOOH and NOOH.

thereby inhibiting the Fe site from functioning as an active center due to OH* coverage.[32] However, Fe sites in $Fe_{0.5}$NiOOH mitigated this by enabling OH* spillover from NiOOH to Fe, lowering OH* coverage on NiOOH, and suppressing the competing OER.[40] Prior studies have emphasized the synergistic effect of FeNi in promoting molecular adsorption and activation to enhance the rate of electrooxidation.[41] On this basis, Fe–Ni catalysts in this work modulate the OH* coverage of the Ni sites by the hydroxyl spillover effect of Fe sites to effectively inhibit the C–C bond cleavage induced by excess OH* at the Ni sites. This mechanism preserved glutaraldehyde adsorption on the Ni site, thereby improving GA selectivity. The synergistic Fe–Ni interaction thus optimizes both activity and selectivity in the electro-oxidation process.

DFT calculations corroborated the proposed glutaraldehyde oxidation reaction (GOR) mechanism (Fig. S28†). The optimized geometries of intermediates on NiOOH (Fig. S29 and S30†) and $Fe_{0.5}$NiOOH (Fig. 5e) surfaces outline the reaction pathway, with the Gibbs free energy diagram (Fig. 5f). Glutaraldehyde undergoes hydration to form $(HO)_2HC(CH_2)_3CH(OH)_2$*, followed by O–H bond dehydrogenation in alkaline solution, yielding $O(OH)HC(CH_2)_3CH(OH)O$*. Subsequent C–H bond cleavage generates $HOOC(CH_2)_3COOH$*, the final glutaric acid (GA) product. $Fe_{0.5}$NiOOH exhibits a lower rate-determining step (RDS) energy barrier (1.97 eV) compared to NiOOH, confirming enhanced O–H dehydrogenation efficiency. Raman analysis revealed that hydroxyl spillover from NiOOH to Fe sites reduces OH* coverage on NiOOH, suppressing excessive OH*-induced C–C cleavage and over-oxidation (Fig. 5g). This modulation lowers the energy barrier and optimizes the RDS thermodynamics. The C–C bond dissociation energy of Ni/CF is a more negative value of −1.07 eV, indicating that the C–C bond dissociates easily (Fig. 5h).[21] The C–C bond dissociation energy in $Fe_{0.5}$NiOOH further confirms resistance to cleavage, highlighting the role of Fe in inhibiting multi-carbon aldehyde degradation.[42] According to the Brønsted–Evans–Polanyi (BEP) relationship, the enhancement of the intermediate binding strength promotes the C–C bond cleavage.[43] Bader charge analysis demonstrated weaker charge transfer from $Fe_{0.5}$NiOOH (0.305–0.314 e^-) to the $*OHC(CH_2)_3CHO$ intermediate compared to NiOOH (0.337–0.347 e^-), correlating with longer bond lengths (1.799–1.802 Å *vs.* 1.793–1.795 Å for NiOOH) (Fig. S31a–d†). Previous studies have shown that the longer bond length between the catalyst and intermediate indicates weaker binding between the catalyst and the intermediate.[44,45] The moderated adsorption strength to the intermediates also effectively avoids deep oxidation and ensures selectivity. These metrics confirm that Fe incorporation moderates intermediate adsorption strength, facilitating desorption and improving selectivity.[44,45] Together, these findings elucidate how $Fe_{0.5}$-NiOOH balances activity and selectivity by regulating hydroxyl coverage, adsorption energetics, and intermediate stability.

Density functional theory (DFT) calculations elucidated the hydrogen evolution reaction (HER) mechanism under alkaline conditions for $Fe_{0.5}$Ni/CF, Fe/CF, and Ni/CF catalysts. The HER proceeds *via* H_2O adsorption on catalyst sites, followed by electrochemical splitting into H* and OH^- (Volmer step: $H_2O + e^- \rightarrow H^* + OH^-$) and subsequent H_2 release through H* recombination (Heyrovsky step: $H^* + H_2O + e^- \rightarrow H_2 + OH^-$).[46,47] Activation energies for H_2O dissociation (Fig. S32a†) and H* adsorption Gibbs free energy (ΔG_H*, Fig. S32b†) were analyzed, with ΔG_H* near 0 eV indicating optimal HER performance.[48] Fe/CF exhibited the lowest H_2O dissociation activation energy but a significantly higher ΔG_H*, hindering H_2 desorption and impairing HER efficiency. In contrast, $Fe_{0.5}$Ni/CF balanced H_2O dissociation and H* adsorption, with ΔG_H* closer to 0 eV due to Fe-induced electronic structure modulation. This synergy between Fe and Ni not only lowers H_2O dissociation barriers but also optimizes H* adsorption, enhancing bifunctional activity for both the HER and glutaraldehyde oxidation (GOR). Fig. S32c, S33 and S34† reveal the structural models of H_2O and H* absorption at $Fe_{0.5}$Ni/CF, Ni/CF, and Fe/CF, respectively. DFT results thus underscore $Fe_{0.5}$Ni/CF's superior HER performance, driven by tailored intermediate adsorption and efficient H_2 release kinetics.

Conclusions

In this work, we present a commercially viable strategy for electrocatalytic production of glutaric acid (GA) with an energy efficiency (EE) of 55.4% using FeNi electrocatalysts. Our results are supported by DFT calculations and experimental analyses, demonstrating that the hydroxyl spillover mechanism effectively reduces the OH* coverage on the NiOOH site, prevents the over-oxidation of glutaraldehyde, and inhibits C–C bond cleavage. Additionally, the introduction of Fe into NiOOH modulates the electronic structure of the catalyst, thereby lowering the energy barrier of the rate-determining step. In the hydrogen evolution reaction (HER)–glutaraldehyde oxidation reaction (GOR) system, the Fe–Ni bifunctional catalyst exhibits high faradaic efficiencies (FEs) for both the cathodic HER (99.8%) and anodic GOR (92.7%) at a current density of 500 mA cm^{-2}. This precise control of OH* coverage at the atomic level is a novel approach in electrocatalysis, demonstrating our ability to optimize reaction pathways and achieve high energy efficiency in the synthesis of high-value chemicals from waste materials. Our findings highlight the potential of this strategy to address key challenges in industrial electrocatalytic processes.

Data availability

The data supporting this article have been included as part of the ESI.†

Author contributions

L. W. and J. L. supervised the research. J. L. conceived the research. J. H. and Y. Y. designed the experiments. J. H. performed most of the experiments and data analysis. Y. Y. and Y. W. prepared the electrodes and helped with electrochemical measurements. J. C. and G. B. helped analyze physical characterization data. All authors discussed the results and commented on the manuscript.

Conflicts of interest

There are no conflicts to declare.

Acknowledgements

This work was supported by the National Natural Science Foundation of China (52272222), Taishan Scholar Young Talent Program (tsqn201909114, tsqn201909123), and University Youth Innovation Team of Shandong Province (202201010318). The author would also like to thank Shiyanjia Lab for the support of DFT calculations (**https://www.shiyanjia.com**).

References

1 F. Yanqui-Rivera and C. A. Opitz, *Nat. Metab.*, 2023, **5**, 1649–1651.
2 E. Minogue, P. P. Cunha, B. J. Wadsworth, G. L. Grice, S. K. Sah-Teli, R. Hughes, D. Bargiela, A. Quaranta, J. Zurita, R. Antrobus, P. Velica, L. Barbieri, C. E. Wheelock, P. Koivunen, J. A. Nathan, I. P. Foskolou and R. S. Johnson, *Nat. Metab.*, 2023, **5**, 1747–1764.
3 W. Li, L. Ma, X. Shen, J. Wang, Q. Feng, L. Liu, G. Zheng, Y. Yan, X. Sun and Q. Yuan, *Nat. Commun.*, 2019, **10**, 3337.
4 F.-M. Wu, X.-W. Wang, B. Jing, Y.-H. Zhang and M.-F. Ge, *Atmos. Environ.*, 2018, **178**, 286–292.
5 W. Zhang, M.-Y. Rao, Z.-J. Cheng, X.-Y. Zhu, K. Gao, J. Yang, B. Yang and X.-L. Liao, *Chem. Pap.*, 2015, **69**, 716–721.
6 W. R. Leow, Y. Lum, A. Ozden, Y. Wang, D.-H. Nam, B. Chen, J. Wicks, T.-T. Zhuang, F. Li, D. Sinton and E. H. Sargent, *Science*, 2020, **368**, 1228–1233.
7 B. Rausch, M. D. Symes, G. Chisholm and L. Cronin, *Science*, 2014, **345**, 1326–1330.
8 J. Twilton, M. R. Johnson, V. Sidana, M. C. Franke, C. Bottecchia, D. Lehnherr, F. Lévesque, S. M. M. Knapp, L. Wang, J. B. Gerken, C. M. Hong, T. P. Vickery, M. D. Weisel, N. A. Strotman, D. J. Weix, T. W. Root and S. S. Stahl, *Nature*, 2023, **623**, 71–76.
9 S. Gnaim, A. Bauer, H.-J. Zhang, L. Chen, C. Gannett, C. A. Malapit, D. E. Hill, D. Vogt, T. Tang, R. A. Daley, W. Hao, R. Zeng, M. Quertenmont, W. D. Beck, E. Kandahari, J. C. Vantourout, P.-G. Echeverria, H. D. Abruna, D. G. Blackmond, S. D. Minteer, S. E. Reisman, M. S. Sigman and P. S. Baran, *Nature*, 2022, **605**, 687–695.
10 X. Yang, Y. Zhang, P. Sun and C. Peng, *Smart Mol.*, 2024, **2**, e20240019.
11 B. Jin, J. Gao, Y. Zhang and M. Shao, *Smart Mol.*, 2024, **2**, e20230026.
12 Y. Gu, Y. Tan, H. Tan, Y. Han, D. Cheng, F. Lin, Z. Qian, L. Zeng, S. Zhang, R. Zeng, Y. Liu, H. Guo, M. Luo and S. Guo, *Nat. Synth.*, 2025, **4**, 614–621.
13 B.-H. Lee, H. Shin, A. S. Rasouli, H. Choubisa, P. Ou, R. Dorakhan, I. Grigioni, G. Lee, E. Shirzadi, R. K. Miao, J. Wicks, S. Park, H. S. Lee, J. Zhang, Y. Chen, Z. Chen, D. Sinton, T. Hyeon, Y.-E. Sung and E. H. Sargent, *Nat. Catal.*, 2023, **6**, 234–243.
14 L. Fan, Y. Zhao, L. Chen, J. Chen, J. Chen, H. Yang, Y. Xiao, T. Zhang, J. Chen and L. Wang, *Nat. Catal.*, 2023, **6**, 585–595.
15 C. Liu, F. Chen, B.-H. Zhao, Y. Wu and B. Zhang, *Nat. Rev. Chem.*, 2024, **8**, 277–293.
16 S. Wang, H. Feng, T. Liu, Y. Deng, M. Zhang, S. Zhao, J. Han and X. Zhang, *ACS Catal.*, 2024, **14**, 9860–9869.
17 P. Zhou, X. Lv, S. Tao, J. Wu, H. Wang, X. Wei, T. Wang, B. Zhou, Y. Lu, T. Frauenheim, X. Fu, S. Wang and Y. Zou, *Adv. Mater.*, 2022, **34**, 2204089.
18 R. Ge, Y. Wang, Z. Li, M. Xu, S.-M. Xu, H. Zhou, K. Ji, F. Chen, J. Zhou and H. Duan, *Angew. Chem., Int. Ed.*, 2022, **61**, e202200211.
19 M. Govindan, D. Yeom, Y. Choi and D. Kim, *J. Electrochem. Soc.*, 2024, **171**, 033501.
20 X. Liu, H. Ma, M. Zhang, P. Che, Y. Luo, S. Zhang and J. Xu, *ACS Catal.*, 2023, **13**, 11104–11116.
21 Y. Xu, W. Yu, H. Zhang, J. Xin, X. He, B. Liu, F. Jiang and X. Liu, *ACS Catal.*, 2021, **11**, 13001–13019.
22 X. Tang, X. Jia and Z. Huang, *J. Am. Chem. Soc.*, 2018, **140**, 4157–4163.
23 J. Zhang, H. B. Yang, D. Zhou and B. Liu, *Chem. Rev.*, 2022, **122**, 17028–17072.
24 J. T. Mefford, Z. Zhao, M. Bajdich and W. C. Chueh, *Energy Environ. Sci.*, 2020, **13**, 622–634.
25 W. Wang, S. Chen, C. Pei, R. Luo, J. Sun, H. Song, G. Sun, X. Wang, Z. Zhao and J. Gong, *Science*, 2023, **381**, 886–890.
26 Y. Yu, Z. Lv, Z. Liu, Y. Sun, Y. Wei, X. Ji, Y. Li, H. Li, L. Wang and J. Lai, *Angew. Chem., Int. Ed.*, 2024, **63**, e202402236.
27 S. Han, C. Cheng, M. He, R. Li, Y. Gao, Y. Yu, B. Zhang and C. Liu, *Angew. Chem., Int. Ed.*, 2020, **62**, e202216581.
28 Y. Jia, Z. Chen, B. Gao, Z. Liu, T. Yan, Z. Gui, X. Liao, W. Zhang, Q. Gao, Y. Zhang, X. Xu and Y. Tang, *J. Am. Chem. Soc.*, 2023, **146**, 1282–1293.
29 D. R. Smith and R.-S. Wang, *Environ. Health Prev. Med.*, 2006, **11**, 3–10.
30 C. Wei, S. Sun, D. Mandler, X. Wang, S. Z. Qiao and Z. J. Xu, *Chem. Soc. Rev.*, 2019, **48**, 2518–2534.
31 Y.-C. Zhang, M. Zhao, J. Wu, Y. Wang, L. Zheng, F. Gu, J.-J. Zou, J. Gao and X.-D. Zhu, *ACS Catal.*, 2024, **14**, 7867–7876.
32 Y. Gao, C. Yang, F. Sun, D. He, X. Wang, J. Chen, X. Zheng, R. Liu, H. Pan and D. Wang, *Angew. Chem., Int. Ed.*, 2024, **64**, e202415755.
33 X. Ding, D. Liu, P. Zhao, X. Chen, H. Wang, F. E. Oropeza, G. Gorni, M. Barawi, M. García-Tecedor, V. A. de la Peña O'Shea, J. P. Hofmann, J. Li, J. Kim, S. Cho, R. Wu and K. H. L. Zhang, *Nat. Commun.*, 2024, **15**, 5336.
34 B. Yu, S.-Y. Jia, Y. Liu, S.-H. Wu and X. Han, *J. Hazard. Mater.*, 2013, **262**, 701–708.
35 S. Luanwuthi, T. Akkharaamnuay, A. Phukhrongthung and C. Puchongkawarin, *Green Chem.*, 2024, **26**, 9209–9219.
36 Y. Yao, G. Zhao, X. Guo, P. Xiong, Z. Xu, L. Zhang, C. Chen, C. Xu, T.-S. Wu, Y.-L. Soo, Z. Cui, M. M.-J. Li and Y. Zhu, *J. Am. Chem. Soc.*, 2024, **146**, 15219–15229.
37 B. Kim, M. K. Kabiraz, J. Lee, C. Choi, H. Baik, Y. Jung, H.-S. Oh, S.-I. Choi and K. Lee, *Matter*, 2021, **4**, 3585–3604.

38 C.-W. Wang, Y. Sun, L.-J. Wang, W.-H. Feng, Y.-T. Miao, M.-M. Yu, Y.-X. Wang, X.-D. Gao, Q. Zhao, Z. Ding, Z. Feng, S.-M. Yu, J. Yang, Y. Hu and J.-F. Wu, *Appl. Catal., B*, 2023, **329**, 122549.
39 Y. Li, Y. Wu, M. Yuan, H. Hao, Z. Lv, L. Xu and B. Wei, *Appl. Catal., B*, 2022, **318**, 121825.
40 Y. Shen, X.-L. Zhang, M.-R. Qu, J. Ma, S. Zhu, Y.-L. Min, M.-R. Gao and S.-H. Yu, *Nat. Commun.*, 2024, **15**, 7861.
41 Y. Hao, D. Yu, S. Zhu, C.-H. Kuo, Y.-M. Chang, L. Wang, H.-Y. Chen, M. Shao and S. Peng, *Energy Environ. Sci.*, 2023, **16**, 1100–1110.
42 I. Jasper, T. L. Valério, V. Klobukoski, C. M. Pesqueira, J. Massaneiro, L. P. Camargo, L. H. Dall' Antonia and M. Vidotti, *Chemosensors*, 2023, **11**, 261.
43 Q. Chang, S. Kattel, X. Li, Z. Liang, B. M. Tackett, S. R. Denny, P. Zhang, D. Su, J. G. Chen and Z. Chen, *ACS Catal.*, 2019, **9**, 7618–7625.
44 L. Xie, J. Wang, K. Wang, Z. He, J. Liang, Z. Lin, T. Wang, R. Cao, F. Yang, Z. Cai, Y. Huang and Q. Li, *Angew. Chem., Int. Ed.*, 2024, e202407658.
45 H. Zhang, X. Wang, Y. Sun, X. Wang, Z. Tang, S. Li, X. Gao, J. Wang, Z. Hou, K. Nie, J. Xie, Z. Yang and Y.-M. Yan, *Appl. Catal., B*, 2024, **351**, 123992.
46 Y. Gu, N. Nie, J. Liu, Y. Yang, L. Zhao, Z. Lv, Q. Zhang and J. Lai, *EcoEnergy*, 2023, **1**, 405–413.
47 M. S. A. Sher Shah, G. Y. Jang, K. Zhang and J. H. Park, *EcoEnergy*, 2023, **1**, 344–374.
48 Y. Li, X. Tan, R. K. Hocking, X. Bo, H. Ren, B. Johannessen, S. C. Smith and C. Zhao, *Nat. Commun.*, 2020, **11**, 2720.